

## Research Paper

## Particle-to-surface frictional contact algorithm for material point method using weighted least squares

Keita Nakamura<sup>\*</sup>, Satoshi Matsumura, Takaaki Mizutani

Port and Airport Research Institute, 3-1-1 Nagase, Yokohama, Kanagawa 239-0826, Japan

## ARTICLE INFO

## Keywords:

Material point method  
Frictional contact  
Particle-to-surface contact  
Weighted least squares  
Penalty method  
Rigid body

## ABSTRACT

This study presents a new particle-to-surface frictional contact algorithm for the material point method (MPM) to simulate the interaction between material points and rigid bodies. Although a grid-based multivelocity field technique is a common method that works well with MPM, there are several disadvantages in developing such simulations: (1) The technique needs additional treatment to prevent early contact and satisfy the impenetrability condition. (2) The method performs poorly in the contact detection of rigid bodies, as it depends on the arrangement of their constituent material points. To overcome these problems, the proposed algorithm uses the penalty method based on particle-to-surface contact. However, the possibility of physical quantities being transferred from the particles to grid nodes located within the rigid bodies arises since a particle can be very close to the surface. The weighted least squares approximation could effectively handle this problem, without forfeiting the partition-of-unity property while constructing the shape function, and is thus incorporated into the MPM framework in this study. The proposed algorithm is validated by comparing numerical simulations with analytical solutions and FEM results. The numerical results show that the proposed algorithm produces reasonable results for frictional contact phenomena.

## 1. Introduction

Meshfree methods have been extensively used for numerical computations and analyses in solid mechanics. A significant advantage of these methods is that they can simulate extremely large deformations—those that cause mesh distortion in the finite element method (FEM). The material point method (MPM) (Sulsky et al., 1994; Sulsky et al., 1995), a popular particle-based method, was developed as an extension of the particle-in-cell (PIC) method (Harlow, 1964). In the MPM, a continuum body is discretized into particles that move through the background mesh. Information pertaining to the physical quantities of the particles, such as velocity and stress, are transferred to the background mesh. The mesh, where the momentum equation is solved, is then deformed based on the updated velocity at nodes. Subsequently, the particle information is updated based on the deformation of the mesh. At the end of the timestep, the deformed mesh is reset to its original state. As the accuracy of MPM simulations is highly dependent on that of the information transfer between the particles and grid, several improvements on the method have been investigated. For example, the original MPM (Sulsky et al., 1994) suffers from a cell-

crossing problem due to the lack of smoothness in the shape function. Bardenhagen and Kober (2004) solved this by developing the generalized interpolation material point (GIMP) method. Steffen et al. (2008) demonstrated MPM simulations with B-spline functions, which are kernel functions extensively used in smooth particle hydrodynamics (SPH) (Monaghan and Lattanzio, 1985). As an extension of the GIMP, Sadeghirad et al. (2011) developed convected particle domain interpolation (CPDI). Although these methods can successfully improve the transfer accuracy between the particles and grid, the angular momentum is still not conserved (Jiang et al., 2015). To address this problem, Klár et al. (2016) applied an affine transfer (Jiang et al., 2015) to sand simulations. In addition, a more general form of the affine transfer algorithm was developed using the weighted least squares (WLS) approximation (Hu et al., 2018). On the other hand, Tran et al. (2019) incorporated a Gaussian quadrature in the cell while applying the moving least squares approximation.

In various engineering problems, as contact phenomena need to be considered, several frictional contact algorithms have been proposed. The grid-based algorithm proposed by Bardenhagen et al. (2000) was a pioneering work, in which the multivelocity field technique was used

<sup>\*</sup> Corresponding author.

E-mail address: [nakamura-ke@p.mpat.go.jp](mailto:nakamura-ke@p.mpat.go.jp) (K. Nakamura).

<https://doi.org/10.1016/j.compgeo.2021.104069>

Received 14 October 2020; Received in revised form 17 January 2021; Accepted 11 February 2021

Available online 23 March 2021

0266-352X/© 2021 The Authors. Published by Elsevier Ltd. This is an open access article under the CC BY license (<http://creativecommons.org/licenses/by/4.0/>).

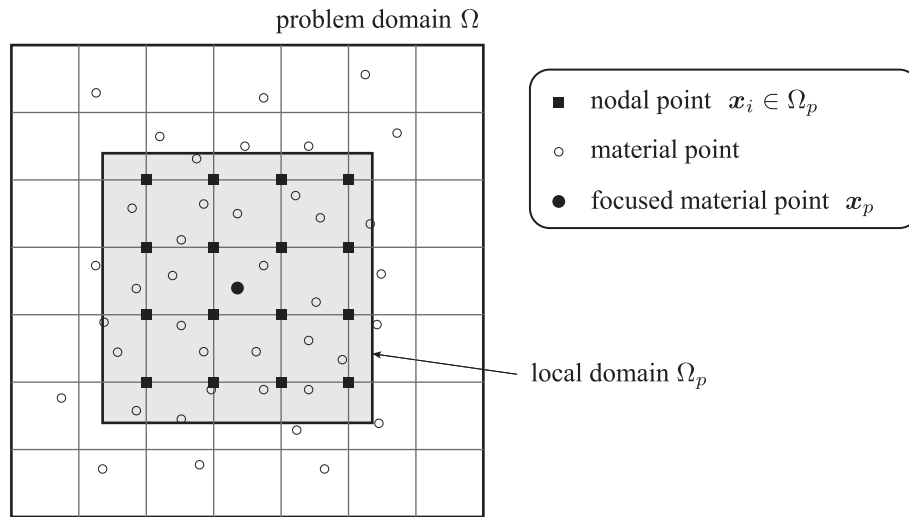


Fig. 1. Problem domain  $\Omega$ , local domain  $\Omega_p$  for material point  $x_p$ , and nodes  $x_i$  in local domain  $\Omega_p$ . WLS is performed for sample points  $x_i$  in  $\Omega_p$ .

with the Coulomb friction model. Bardenhagen et al. (2001) improved upon this algorithm by considering normal traction as the contact criterion. A local multimesh contact method (Ma et al., 2010) was also proposed to reduce computational storage and cost. However, as indicated by Lemiale et al. (2010), this algorithm (Bardenhagen et al., 2000) was found to detect contact before the bodies were actually in contact because two bodies are identified to be in contact when physical quantities, such as velocity, are mapped to the same grid node. This becomes a critical problem, particularly when high-order shape functions with large support domains are used. To solve this problem, Lemiale et al. (2010) and Nairn (2013) used the volume gradient and an additional criterion by extrapolating the positions from the particles to the grid. In addition, Ma et al. (2014) introduced a penalty function to improve contact detection.

Although these methods improve the accuracy of the contact algorithm, the impenetrability condition may be violated. As particle motion is implicitly solved using the background grid, satisfying the impenetrability condition at the grid node does not always guarantee the same for the condition of the particles. Huang et al. (2011) attempted to solve this problem by imposing contact constraints on the redefined as well as deformed grid. Another simple way of dealing with this problem is by applying the penalty method. While the penalty method weakly satisfies the kinematic constraints, it continues to impose constraints until the impenetrability condition is recovered. Hamad et al. (2017) used the penalty method to improve contact detection in the CPDI (Sadeghirad et al., 2011). The penalty method is simple, but the calculation results depend on the selection of appropriate penalty parameter. Thus, other approaches have also been proposed such as the augmented Lagrangian technique (Simo and Laursen, 1992; Chen et al., 2017) and the variational inequality theory (Jiang and Zheng, 2011; Zheng et al., 2016).

In the above algorithms for the MPM, the continuum bodies are composed of material points. In contrast, a contact algorithm—where one of the two bodies is structured by its surface rather than particles—has also been studied and is suitable for simulating the interaction between soft materials and rigid or deformable structures. These algorithms were developed for MPM-FEM (Lian et al., 2011; Chen et al., 2015; Cheon and Kim, 2018) and material point method-discrete element method (MPM-DEM) (Liu et al., 2018) coupled simulations. Additionally, Hu et al. (2018) demonstrated MPM-rigid body coupled simulations.

In this study, we present a simple approach, considering the frictional contact between the MPM and rigid bodies. Previous algorithms (e.g., Bardenhagen et al. (2000)) detected contact using the background mesh, whereas the proposed algorithm performs contact detection using

the penalty method directly between the particle and surface of the rigid body (i.e., particle-to-surface contact algorithm). Hence, precise contact detection is achieved, even for high-order shape functions. However, this leads to an inconsistency, wherein the physical quantities may be transferred from the particles to the grid nodes located within the rigid bodies, which cannot be solved by simply ignoring such invalid nodes in an attempt to retain the partition-of-unity property. Therefore, in this study, the WLS approximation is employed to construct the shape function (Hu et al., 2018) for valid nodes. Construction of shape functions using the least squares principle has been extensively applied in other meshfree methods such as the element-free Galerkin methods (EFG) (Belytschko et al., 1994) and the reproducing kernel particle method (RKPM) (Liu et al., 1995). As the proposed approach is based on the particle-to-surface contact algorithm, it is also compatible with MPM-DEM or MPM-FEM coupled simulations, which we intend to explore in future research.

The remainder of this paper is organized as follows: Section 2 elucidates the WLS scheme for the MPM, Section 3 presents an overview of material point discretization, Section 4 details the new particle-to-surface contact algorithm, and Section 5 describes the numerical implementation of the WLS-MPM with the proposed frictional contact algorithm. The proposed formulation is validated through three types of numerical simulation in Section 6. Lastly, Section 7 provides the conclusion and the scope for future work.

The notations and symbols used in the paper are as follows: bold-face letters denote vectors and matrices; symbol ‘ $\cdot$ ’ denotes a single contraction of adjacent indices (e.g.,  $a \cdot b = a_i b_i$ ,  $c \cdot a = c_{ij} a_j$  and  $c \cdot d = c_{ij} d_{jk}$ ); symbol ‘ $\cdot\cdot$ ’ denotes a double contraction of adjacent indices (e.g.,  $A : B = A_{ij} B_{ij}$  and  $C : A = C_{ijkl} A_{kl}$ ); symbol ‘ $\otimes$ ’ denotes a tensor product (e.g.,  $a \otimes b = a_i b_j$ ).

## 2. Weighted least squares approximation

In this section, we introduce the WLS scheme for the MPM (WLS-MPM), proposed by Hu et al. (2018). Although this method was named the moving least squares material point method (MLS-MPM), we refer to it as the WLS-MPM in this study because the coefficients of the polynomials depend on a fixed point, rather than an arbitrary point like the MLS. The proposed WLS scheme in the MPM includes two parts: (1) Local approximation using WLS and (2) global approximation combining the local fits based on the partition-of-unity method (Shepard’s method; Shepard (1968)).

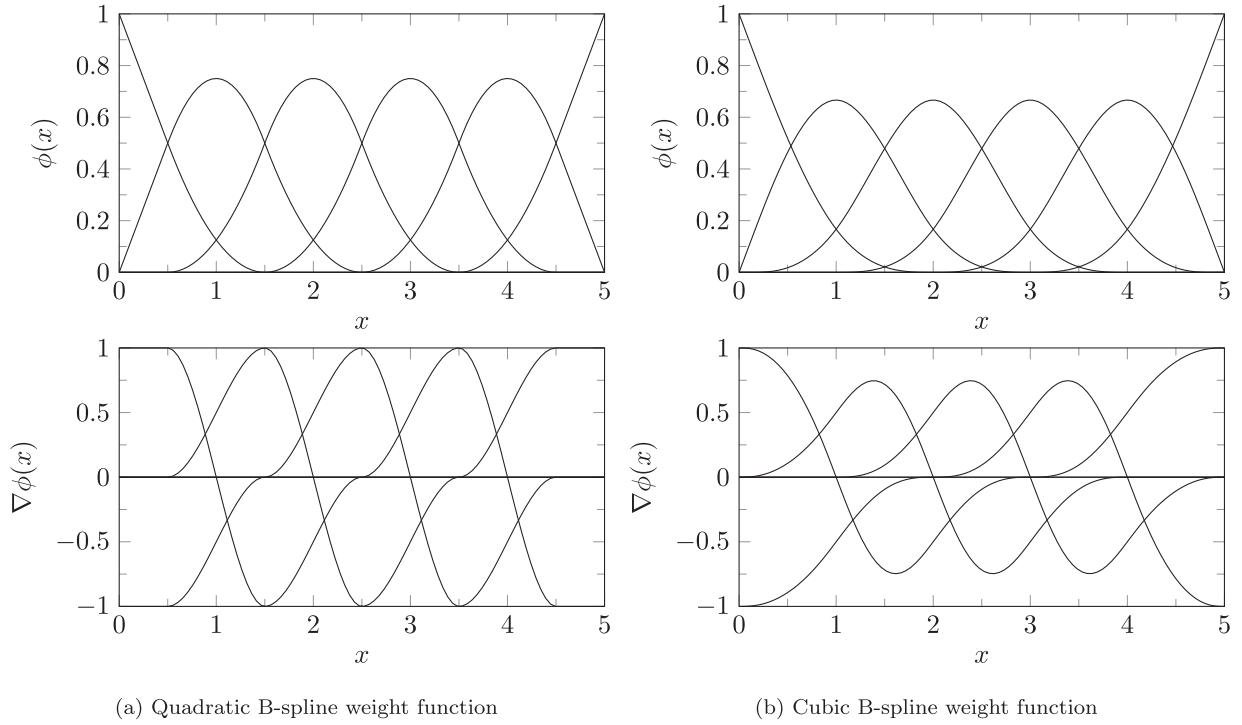


Fig. 2. WLS shape function and its gradient with a linear polynomial and B-spline weight function.

### 2.1. Local approximation using weighted least squares

Given a continuum body comprising particles located at  $\mathbf{x}_p$  in the problem domain  $\Omega$ , in the WLS scheme, the local distribution of function  $u$  around  $\mathbf{x}_p$  can be approximated by

$$\tilde{u}_p(\mathbf{x}) = \sum_j^m c_j(\mathbf{x}_p) p_j(\mathbf{x} - \mathbf{x}_p) \equiv \mathbf{c}(\mathbf{x}_p) \cdot \mathbf{p}(\mathbf{x} - \mathbf{x}_p), \quad (1)$$

where  $\mathbf{p}$  is a complete polynomial basis and  $\mathbf{c}$  is the coefficient vector. In three dimensions, for instance, a linear polynomial can be represented as follows:

$$\mathbf{p}^T(\mathbf{x}) = [1, x, y, z], \quad m = 4. \quad (2)$$

The undetermined vector  $\mathbf{c}$  can be obtained by minimizing a weighted discrete  $L_2$  norm, defined as

$$J_p(\mathbf{c}) = \sum_i w_i(\mathbf{x}_p) [\mathbf{c}(\mathbf{x}_p) \cdot \mathbf{p}(\mathbf{x}_i - \mathbf{x}_p) - u_i]^2, \quad (3)$$

where  $w_i(\mathbf{x}_p) = w(\mathbf{x}_p - \mathbf{x}_i)$  is the weight function and  $u_i$  is the value of function  $u$  at sample point  $\mathbf{x}_i$ . The weight function should decrease as the distance from  $\mathbf{x}_i$  to  $\mathbf{x}_p$  increases, so that well-known weight functions such as the B-spline functions may be applied. We define local domain  $\Omega_p$  satisfying  $w_i(\mathbf{x}_p) \neq 0$  (which is, in general, rectangular parallelepiped in the MPM). This domain can be regarded as the support domain of a particle in accordance with the element-free Galerkin (EFG) (Belytschko et al., 1994) method and the SPH method (Monaghan and Lattanzio, 1985). As shown in Fig. 1, the grid nodes assume the role of fixed sample points  $\mathbf{x}_i$ .

Solving for  $\mathbf{c}(\mathbf{x}_p)$  by minimizing  $J_p$  in Eq. (3),

$$\mathbf{c}(\mathbf{x}_p) = \sum_i u_i w_i(\mathbf{x}_p) \mathbf{q}_i(\mathbf{x}_p), \quad (4)$$

where

$$\mathbf{q}_i(\mathbf{x}_p) = \mathbf{M}^{-1}(\mathbf{x}_p) \cdot \mathbf{p}(\mathbf{x}_i - \mathbf{x}_p), \quad (5)$$

and the moment matrix  $\mathbf{M}$  is

$$\mathbf{M}(\mathbf{x}_p) = \sum_i w(\mathbf{x}_p - \mathbf{x}_i) \mathbf{p}(\mathbf{x}_i - \mathbf{x}_p) \otimes \mathbf{p}(\mathbf{x}_i - \mathbf{x}_p). \quad (6)$$

Substituting Eq. (4) in Eq. (1) yields the following expression:

$$\tilde{u}_p(\mathbf{x}) = \sum_i \phi_i(\mathbf{x}) u_i, \quad (7)$$

where  $\phi_i(\mathbf{x})$  are the shape functions for WLS

$$\phi_i(\mathbf{x}) = w_i(\mathbf{x}_p) \mathbf{q}_i(\mathbf{x}_p) \cdot \mathbf{p}(\mathbf{x} - \mathbf{x}_p). \quad (8)$$

The gradient of  $\phi_i$  is

$$\nabla \phi_i(\mathbf{x}) = \frac{\partial \phi_i(\mathbf{x})}{\partial \mathbf{x}} = w_i(\mathbf{x}_p) \mathbf{q}_i(\mathbf{x}_p) \cdot \frac{\partial \mathbf{p}(\mathbf{x} - \mathbf{x}_p)}{\partial \mathbf{x}}. \quad (9)$$

A key aspect of this WLS scheme is that the nodal points  $\mathbf{x}_i$  are used as fixed sample points for local approximation. This reduces the computational cost considerably since the necessity of performing a neighbor particle search is removed. Furthermore, as the coefficient  $\mathbf{c}$  depends on  $\mathbf{x}_p$  instead of  $\mathbf{x}$  (unlike the MLS), only  $\mathbf{p}(\mathbf{x} - \mathbf{x}_p)$  in Eq. (1) depends on  $\mathbf{x}$ , which simplifies the expression for gradient  $\nabla \phi_i(\mathbf{x})$ . If linear basis (2) is applied to Eq. (1),  $\nabla_x \mathbf{p}(\mathbf{x} - \mathbf{x}_p)$  in Eq. (9) becomes constant, which no longer necessitates the evaluation of the gradient of weight function  $\nabla_x w_i(\mathbf{x}_p)$ , as stated by Hu et al. (2018).

**Remark 1.** Generally, WLS approximations forfeit the Kronecker delta property  $u(\mathbf{x}_i) \neq u_i$ , leading to difficulties in enforcing essential boundary conditions. The presented WLS scheme can handle this problem with the following approach: For example, when the  $n$  order polynomial basis in 1D is considered, the local domain  $\Omega_p$  of the particle needs to cover at least  $n+1$  nodes for the WLS. More specifically, if the number of nodes in  $\Omega_p$  is  $n+1$  when the particle is located on the boundary, a polynomial fit of order  $n$  exactly interpolates the function  $u$ ; hence, the Kronecker delta property is recovered on the boundary, as shown in Fig. 2. Consequently, the WLS-MPM does not require any special treatment, unlike other meshless methods (e.g., Mukherjee and

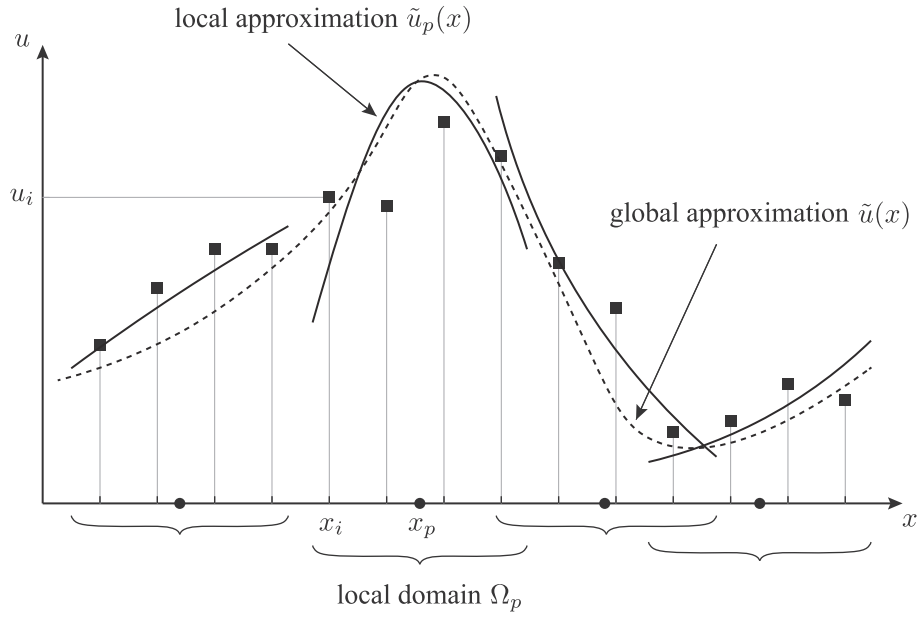


Fig. 3. Global approximation reconstructed from local approximations.

Mukherjee (1997)), and can appropriately handle the essential boundary conditions, similar to the original MPM.

## 2.2. Global approximation using the partition of unity

We now have a set of local approximations  $\tilde{u}_p(x)$  in  $\Omega_p$ . Following this, we construct a global approximation by combining the local approximations for the function reconstruction of  $u$ . As the local approximations overlap and are generally not continuous with each other, an appropriate procedure needs to be adopted. In this study, we select the Shepard's method (Shepard, 1968), which enables the extension of local approximations to cover the entire domain based on the weighted average (Fig. 3). Defining the Shepard interpolation function  $\psi_p$ , the global approximation can be expressed as

$$\tilde{u}(x) = \sum_p \psi_p(x) \tilde{u}_p(x) = \sum_p \psi_p(x) c(x_p) \cdot p(x - x_p), \quad (10)$$

where

$$\psi_p(x) = \frac{w(x_p - x)}{\sum_q w(x_q - x)}. \quad (11)$$

For example, Sulsky et al. (1994) and Hu et al. (2018) used a function weighted by material point mass  $m_p$  as the weighted function:

$$\psi_p(x) = \frac{w(x_p - x)m_p}{\sum_q w(x_q - x)m_q}. \quad (12)$$

A key difference between the WLS-MPM and the original MPM is that the former uses local approximation  $\tilde{u}_p(x)$ , instead of  $u_p$ , for the function reconstruction, i.e.,  $\tilde{u}(x) = \sum_p \psi_p(x) \tilde{u}_p$  with Eq. (12) is applied in the original MPM.

## 3. Overview of MPM discretization

In this section, we briefly present an overview of MPM discretization. The only difference between this method and the original MPM (Sulsky et al., 1994) is the application of the WLS shape function in the formulations.

### 3.1. Governing equations

In the problem domain  $\Omega$ , the conservation of momentum in the Eulerian form is given by

$$\rho \dot{\mathbf{v}} = \nabla \cdot \boldsymbol{\sigma} + \rho \mathbf{b}, \quad (13)$$

where  $\rho$  is the mass density,  $\mathbf{b}$  is the body force per unit mass,  $\boldsymbol{\sigma}$  is the Cauchy stress, and the superposed dot denotes the material derivative. The boundary conditions are

$$\boldsymbol{\sigma} \cdot \mathbf{n} = \bar{\mathbf{t}} \quad \text{on } \partial\Omega_t, \quad (14)$$

$$\mathbf{v} = \bar{\mathbf{v}} \quad \text{on } \partial\Omega_v, \quad (15)$$

where the superposed bar denotes the prescribed boundary values and  $\mathbf{n}$  is the unit normal to the body surface  $\partial\Omega$ .

The weak form of the conservation of momentum becomes

$$\int_{\Omega} \boldsymbol{\eta} \cdot \rho \dot{\mathbf{v}} dV = \int_{\Omega} \nabla \boldsymbol{\eta} : \boldsymbol{\sigma} dV + \int_{\Omega} \boldsymbol{\eta} \cdot \rho \mathbf{b} dV + \int_{\partial\Omega_t} \boldsymbol{\eta} \cdot \bar{\mathbf{t}} dA, \quad (16)$$

where  $\boldsymbol{\eta}$  denotes the vector-valued test function. Note that conservation of mass is automatically satisfied in the MPM (Sulsky et al., 1994).

### 3.2. Space discretization

From Eq. (16), the continuum domain is divided into local domains  $\Omega_p$  as

$$\sum_p \int_{\Omega_p} \boldsymbol{\eta} \cdot \rho \dot{\mathbf{v}} dV = \sum_p \int_{\Omega_p} \nabla \boldsymbol{\eta} : \boldsymbol{\sigma} dV + \sum_p \int_{\Omega_p} \boldsymbol{\eta} \cdot \rho \mathbf{b} dV + \sum_p \int_{\partial\Omega_{tp}} \boldsymbol{\eta} \cdot \bar{\mathbf{t}} dA. \quad (17)$$

Based on the WLS approximation, the velocity  $\mathbf{v}$  and test function  $\boldsymbol{\eta}$  can be interpolated from the nodal velocity  $\mathbf{v}_i$  and nodal test function  $\boldsymbol{\eta}_i$ , respectively:

$$\mathbf{v} = \tilde{\mathbf{v}}_p(x) = \sum_i \phi_i(x) \mathbf{v}_i, \quad (18)$$

$$\boldsymbol{\eta} = \tilde{\boldsymbol{\eta}}_p(x) = \sum_i \phi_i(x) \boldsymbol{\eta}_i. \quad (19)$$

Thus, Eq. (17) for the local domain  $\Omega_p$  becomes

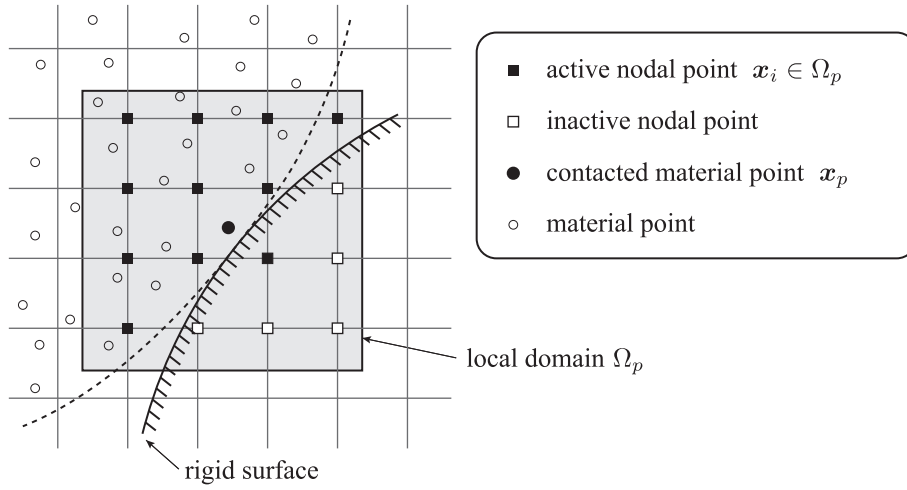


Fig. 4. Deactivated grid nodes excluded from the construction of the shape functions in local domain  $\Omega_p$ .

$$\sum_i \eta_i \cdot \sum_j \left[ \int_{\Omega_p} \phi_i \phi_j \rho dV \right] \dot{v}_j = \sum_i \eta_i \cdot \left[ \int_{\Omega_p} \nabla \phi_i \cdot \sigma dV + \int_{\Omega_p} \phi_i \rho b dV + \int_{\partial \Omega_p} \phi_i \bar{t} dA \right]. \quad (20)$$

Invoking the arbitrariness of  $\eta_i$ ,

$$\sum_j m_{ij} \dot{v}_j = f_i^{\text{int}} + f_i^{\text{ext}}, \quad (21)$$

where

$$m_{ij} = \sum_p \int_{\Omega_p} \phi_i \phi_j \rho dV = \sum_p m_p \phi_i(x_p) \phi_j(x_p), \quad (22)$$

$$f_i^{\text{int}} = \sum_p \int_{\Omega_p} \nabla \phi_i \cdot \sigma dV = \sum_p V_p \nabla \phi_i(x_p) \cdot \sigma_p, \quad (23)$$

$$f_i^{\text{ext}} = \sum_p \left[ \int_{\Omega_p} \phi_i \rho b dV + \int_{\partial \Omega_p} \phi_i \bar{t} dA \right] = \sum_p \phi_i(x_p) m_p b_p + \bar{f}_i. \quad (24)$$

Here,  $m_{ij}$  is called a consistent mass matrix. In the MPM, a lumped mass matrix is used instead of a consistent mass matrix in order to simplify the computations (Sulsky et al., 1994). The lumped mass matrix is a diagonal matrix, in which each diagonal entry is the corresponding row sum of the consistent matrix, which takes the following form:

$$m_i = \sum_p \int_{\Omega_p} \phi_i \rho dV = \sum_p m_p \phi_i(x_p). \quad (25)$$

### 3.3. Time discretization

Applying the forward Euler time discretization to Eq. (21), and using the lumped mass matrix in Eq. (25),

$$v_{i,n+1} = v_{i,n} + \Delta t \frac{f_{i,n}^{\text{int}} + f_{i,n}^{\text{ext}}}{m_{i,n}}, \quad (26)$$

where subscript  $n$  denotes the time step and  $\Delta t = t_{n+1} - t_n$ .

## 4. Contact algorithm

In this section, we present a new contact algorithm based on the penalty method for MPM–rigid body coupled simulations. Although the penalty method satisfies the kinematic constraints in a weak sense, it has been extensively applied for numerical calculations because of its simplicity. The procedure for the proposed algorithm is as follows: (1)

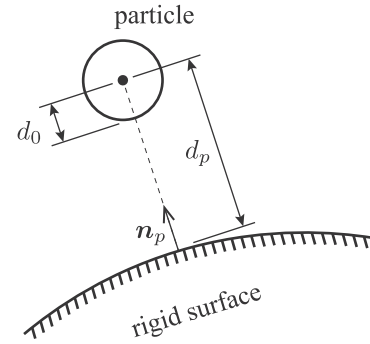


Fig. 5. Particle-to-surface contact method. Contact is detected, when  $d_p - d_0 < 0$ .

Initially, the normal contact force  $f_i^{\text{c,nor}}$  is computed at the particle, following the particle-to-surface contact algorithms, after which, the force is mapped to the grid node. This approach enables more precise contact detection compared to the purely grid-base algorithms (e.g., Bardenhagen et al. (2000, 2001)), particularly when using high-order shape functions. In this case, however, as the particle can be very close to the surface, it is necessary to handle the overlapped domain between the particle domain  $\Omega_p$  and the rigid body. More specifically, the physical quantities may be transferred from the particles to the grid node located within the rigid body. We address this problem by deactivating and ignoring the nodes within the rigid body during the construction of the shape functions. As we use the WLS approximation in local domain  $\Omega_p$ , the partition of unity property continues to hold. Therefore, physical quantity transfer between the particles and grid can be appropriately performed. (2) Unlike the normal contact force, the tangential component  $f_i^{\text{c,tan}}$  is directly computed at the grid nodes to satisfy their exact frictional constraints based on the Coulomb friction. (3) The updated nodal velocity in Eq. (26) further needs to be modified using the calculated contact force  $f_i^{\text{c}} = f_i^{\text{c,nor}} + f_i^{\text{c,tan}}$ . Detailed descriptions of the above are provided in the following sections.

### 4.1. Shape function and its gradient for the particles in contact

The shape function and its gradient need to be suitably treated for the particles contacting the rigid bodies because of the overlap of the particle domain  $\Omega_p$  with the rigid bodies. As shown in Fig. 4, the grid nodes within the rigid bodies should be deactivated, i.e., they need to be excluded from the construction of the shape function (Eqs. (8) and (9) or

Eqs. (37) and (38)). However, to appropriately advect the particles during grid-to-particle transfer, the grid nodes surrounding the contacted particles need to be activated, even if they are within the rigid bodies.

#### 4.2. Normal contact force and rigid body velocity

The normal contact force is computed based on the distance between particle  $p$  and the rigid surface. Using distance  $d_p$  (Fig. 5), the contact distance  $d$  can be obtained as

$$d = d_p - d_0, \quad (27)$$

where  $d_0$  is the contact detection threshold (contact occurs, if  $d = d_p - d_0 < 0$ ). The threshold distance can be considered as  $l_p$ , where  $2l_p$  is the particle size. In 1D, for example, if  $N_p$  particles are aligned in the grid spacing  $h$ , the particle size becomes  $2l_p = h/N_p$ . Although, strictly, the particle size should be the current particle size and the shape of the particle should not be spherical (e.g., a rectangle in 2D), we use the initial size and consider a spherical particle for contact detection because of its simplicity. Note that to effectively find the particles in contact, only particles with deactivated nodes in local domain  $\Omega_p$  need to be checked by using Eq. (27).

The normal contact force is calculated based on the penetration distance  $d$  as

$$f_p^{c,nor} = -k^{nor} d n_p, \quad (28)$$

where  $k^{nor}$  is the penalty stiffness parameter depending on the material stiffness. Based on the numerical simulations (discussed in Section 6.1), the calculation results are sensitive to the penalty stiffness  $k^{nor}$ . To obtain the appropriate stiffness parameter, sensitivity analysis is required as in the other methods based on the penalty method. A more suitable method for calculating the normal contact force is worth investigating.

Finally, the normal contact force  $f_i^{c,nor}$  and the velocity of rigid body  $v_i^{rigid}$  are transferred from the particles in contact as follows:

$$f_i^{c,nor} = \sum_p \phi_i(x_p) f_p^{c,nor}, \quad (29)$$

$$v_i^{rigid} = \sum_p \psi_i(x_p) v_p^{rigid}. \quad (30)$$

#### 4.3. Tangential (frictional) contact force

If there is no friction between the particles and rigid bodies, the tangential component is zero ( $f_i^{c,tan} = 0$ ); hence, the contact force  $f^c$  at node  $i$  is  $f_i^c = f_i^{c,nor}$ . In contrast, if frictional contact is considered, the tangential component is evaluated based on the Coulomb friction. We first calculate the tangential force for the stick condition, where the particle velocity coincides with the rigid body velocity. As the relative velocity between the particle and rigid surface is

$$\hat{v}_i = v_i - v_i^{rigid}, \quad (31)$$

the tangential component is

$$\hat{v}_i^{tan} = \hat{v}_i - (\hat{v}_i \cdot \mathbf{n}_i) \mathbf{n}_i, \quad (32)$$

where  $\mathbf{n}_i = f_i^{c,nor} / \|f_i^{c,nor}\|$ . Thus, the tangential force  $f_i^{stick}$  can be computed as

$$f_i^{stick} = -\frac{m_i \hat{v}_i^{tan}}{\Delta t}. \quad (33)$$

Considering Coulomb friction leads to the following tangential (frictional) force:

$$f_i^{c,tan} = \min(\mu \|f_i^{c,nor}\|, \|f_i^{stick}\|) \frac{f_i^{stick}}{\|f_i^{stick}\|}. \quad (34)$$

Note that the force for the stick condition (33) is computed assuming that the motion of the rigid body is given and known. Therefore, another form is needed in order to perform a two-way coupling simulation between the MPM and rigid bodies. For example, the most simple form may become  $f_i^{stick} = -k^{tan} \hat{v}_i^{tan} \Delta t$ , where  $k^{tan}$  is the penalty stiffness in the tangential direction. See Wang and Chan (2014) for a more detailed implementation.

### 5. Numerical implementation of the WLS-MPM considering frictional contact

In this section, we derive the detailed step-by-step numerical implementation of the WLS-MPM in a timestep.

#### 5.1. Shape function and its gradient

For the weight function  $w$ , we use the cubic B-spline function in this study:

$$w_i(\mathbf{x}) = N\left(\frac{x - x_i}{h}\right) N\left(\frac{y - y_i}{h}\right) N\left(\frac{z - z_i}{h}\right), \quad (35)$$

where  $h$  is the grid spacing, and  $N$  is defined as

$$N(\xi) = \frac{1}{6} \begin{cases} 3|\xi|^3 - 6|\xi|^2 + 4 & 0 \leq |\xi| < 1 \\ (2 - |\xi|)^3 & 1 \leq |\xi| < 2 \\ 0 & 2 \leq |\xi| \end{cases} \quad (36)$$

The shape function (8) and its gradient (9) at position  $x_{p,n}$  can be expressed, respectively, as

$$\phi_i(x_{p,n}) = w_i(x_{p,n}) \mathbf{q}_i(x_{p,n}) \cdot \mathbf{p}_0, \quad (37)$$

$$\nabla \phi_i(x_{p,n}) = w_i(x_{p,n}) \mathbf{q}_i(x_{p,n}) \cdot \nabla \mathbf{p}_0, \quad (38)$$

where  $\mathbf{p}_0 = \mathbf{p}(x - x_{p,n})|_{x=x_{p,n}}$ . As mentioned by Hu et al. (2018), the WLS-MPM does not require the computation of  $\nabla w_i(\mathbf{x})$  for the gradient of shape function  $\nabla \phi_i$ , which can reduce the computation cost.

#### 5.2. Particle-to-grid transfer

To solve the momentum Eq. (26), we need to compute the lumped mass matrix  $m_i$ , internal force vector  $f_i^{int}$ , and external force vector  $f_i^{ext}$  using Eq. (25), (23), and (24), respectively. The remaining term  $v_{i,n}$  in Eq. (26) can be evaluated through global approximation (see Section 2.2):

$$v_{i,n} = \tilde{v}_n(x_i) = \sum_p \psi_p(x_i) C_{p,n} \mathbf{p}(x_i - x_{p,n}), \quad (39)$$

where  $C_{p,n}$  is a  $d \times m$  coefficient matrix ( $d$  is the dimension in the problem).

If the material point is in contact with a rigid body, the corresponding normal contact force  $f_i^{c,nor}$  and velocity of the rigid body  $v_i^{rigid}$  also need to be computed through Eqs. (29) and (30), respectively, using the values at  $t = t_n$ .

#### 5.3. Updating the nodal velocity

The nodal velocity  $v_i$  is updated using Eq. (26). If contact is detected, i.e., the normal contact force is mapped to the node, the nodal tangential (frictional) contact force  $f_i^{c,tan}$  must be calculated using the Coulomb model (see Eq. (34)), based on the updated nodal velocity in Eq. (26). The nodal contact force can be then computed as  $f_i^c = f_i^{c,nor} + f_i^{c,tan}$ .



Finally, the velocity is further updated as

$$\mathbf{v}_{i,n+1} \leftarrow \mathbf{v}_{i,n+1} + \Delta t \frac{\mathbf{f}_i^c}{m_{i,n}}. \quad (40)$$

#### 5.4. Grid-to-particle transfer

After updating the nodal velocity using Eq. (26) and Eq. (40), we update the physical quantities of the material points. Firstly, the coefficient matrix  $\mathbf{C}$  can be updated as

$$\mathbf{C}_{p,n+1} = \sum_i \mathbf{v}_{i,n+1} \otimes \mathbf{w}_i(\mathbf{x}_{p,n}) \mathbf{q}_i(\mathbf{x}_{p,n}). \quad (41)$$

Following this, the updated velocity of the particle can be obtained as

$$\mathbf{v}_{p,n+1} = \tilde{\mathbf{v}}_{p,n+1}(\mathbf{x}_{p,n}) = \mathbf{C}_{p,n+1} \cdot \mathbf{p}_0 = \sum_i \mathbf{v}_{i,n+1} \phi_i(\mathbf{x}_{p,n}), \quad (42)$$

and its gradient as

$$\nabla \mathbf{v}_{p,n+1} = \nabla \tilde{\mathbf{v}}_{p,n+1}(\mathbf{x}_{p,n}) = \mathbf{C}_{p,n+1} \cdot \nabla \mathbf{p}_0 = \sum_i \mathbf{v}_{i,n+1} \otimes \nabla \phi_i(\mathbf{x}_{p,n}). \quad (43)$$

Using the updated velocity gradient, the deformation gradient can be updated as

$$\mathbf{F}_{p,n+1} = (\mathbf{I} + \Delta t \nabla \mathbf{v}_{p,n+1}) \cdot \mathbf{F}_{p,n}. \quad (44)$$

When the Jaumann rate is selected for the objective stress tensor, the updated stress becomes

$$\boldsymbol{\sigma}_{p,n+1} = \boldsymbol{\sigma}_{p,n} + \mathbf{T} : \Delta \mathbf{d}_p + (\Delta \boldsymbol{\omega}_p \cdot \boldsymbol{\sigma}_{p,n} - \boldsymbol{\sigma}_{p,n} \cdot \Delta \boldsymbol{\omega}_p), \quad (45)$$

where  $\mathbf{T}$  is the tangent modulus tensor of the material model;  $\mathbf{d}$  and  $\boldsymbol{\omega}$  are the rates of the deformation tensor and spin tensor, respectively, which can then be represented as

$$\Delta \mathbf{d}_p = \frac{1}{2} [\nabla \mathbf{v}_{p,n+1} + (\nabla \mathbf{v}_{p,n+1})^T] \Delta t, \quad (46)$$

$$\Delta \boldsymbol{\omega}_p = \frac{1}{2} [\nabla \mathbf{v}_{p,n+1} - (\nabla \mathbf{v}_{p,n+1})^T] \Delta t. \quad (47)$$

Lastly, the position of the particle can be updated as

$$\mathbf{x}_{p,n+1} = \mathbf{x}_{p,n} + \Delta t \mathbf{v}_{p,n+1}. \quad (48)$$

#### 5.5. Critical time-step criterion

The Courant–Friedrichs–Levy condition (CFL) (Courant et al., 1967) must be considered for obtaining a stable solution in explicit time integration. The critical time increment is given by

$$\Delta t_{cr} = \frac{h}{\max_p (c_p + \|\mathbf{v}_p\|)}, \quad (49)$$

where  $h$  is the grid spacing;  $c_p$  and  $\mathbf{v}_p$  are the sound speed and velocity of particle  $p$ , respectively. Subsequently, the sound speed can be calculated by

$$c = \sqrt{\frac{K + \frac{4}{3}G}{\rho}}, \quad (50)$$

where  $K$  is the bulk modulus,  $G$  is the shear modulus, and  $\rho$  is the density. We apply  $\Delta t = 0.5 \Delta t_{cr}$  to the numerical simulations described in Section 6

**Table 1**

Comparison of the MPM and WLS-MPM equations.

	MPM	WLS-MPM
Shape function, $\phi_{ip}$	$w_i(\mathbf{x}_p)$	$w_i(\mathbf{x}_p) \mathbf{q}_i(\mathbf{x}_p) \cdot \mathbf{p}_0$
Shape function gradient, $\nabla \phi_{ip}$	$\nabla w_i(\mathbf{x}_p)$	$w_i(\mathbf{x}_p) \mathbf{q}_i(\mathbf{x}_p) \cdot \nabla \mathbf{p}_0$
Grid mass, $m_i$	$\sum_p \phi_{ip} m_p$	*
Grid internal force, $f_i^{\text{int}}$	$\sum_p V_p \nabla \phi_{ip} \cdot \boldsymbol{\sigma}_p$	*
Grid external force, $f_i^{\text{ext}}$	$\sum_p \phi_{ip} m_p \mathbf{b}_p$	*
Grid velocity, $\mathbf{v}_i$	$\sum_p \psi_p(\mathbf{x}_i) \mathbf{v}_p$	$\sum_p \psi_p(\mathbf{x}_i) \mathbf{C}_p \cdot \mathbf{p}(\mathbf{x}_i - \mathbf{x}_p)$
Particle velocity, $\mathbf{v}_{p,n+1}$	$\mathbf{v}_{p,n} + \Delta t \sum_i \frac{f_i}{m_i} \phi_{ip}$	$\sum_i \mathbf{v}_{i,n+1} \phi_{ip}$
Gradient of the particle velocity, $\nabla \mathbf{v}_{p,n+1}$	$\sum_i \mathbf{v}_{i,n+1} \otimes \nabla \phi_{ip}$	*
Particle position, $\mathbf{x}_{p,n+1}$	$\mathbf{x}_{p,n} + \Delta t \sum_i \mathbf{v}_{i,n+1} \phi_{ip}$	$\mathbf{x}_{p,n} + \Delta t \mathbf{v}_{p,n+1}$
Coefficient matrix for WLS, $\mathbf{C}_{p,n+1}$	–	$\sum_i \mathbf{v}_{i,n+1} \otimes w_i(\mathbf{x}_{p,n}) \mathbf{q}_i(\mathbf{x}_{p,n})$

\* The equation is the same as that of the MPM.

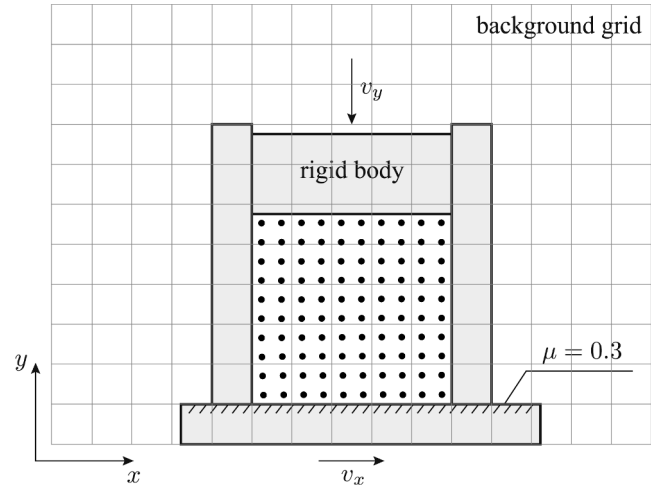


**Fig. 6.** Geometry for the slide-box simulation. All the plates, except the bottom one, are smooth. The material point arrangement is the same as that for a rough mesh ( $h = 0.02$  m).

#### 5.6. Differences in formulation among the three methods: MPM, WLS-MPM, and the method proposed by Hu et al. (2018)

A similar formulation, using the linear polynomial basis and the function weighted by the material point mass for function reconstruction (see Eq. (12)), has been derived by Hu et al. (2018). Therefore, in case the particle is neither close to the boundary nor to the rigid surface,

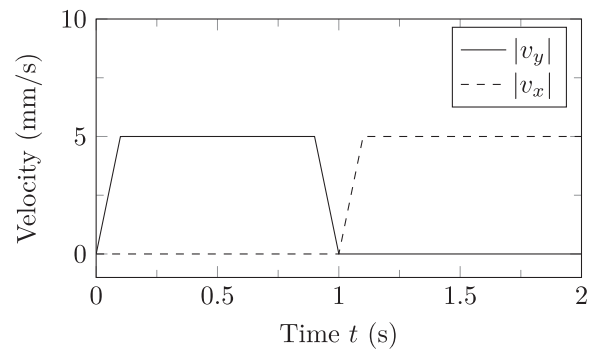


**Fig. 7.** Controlled velocities of the top and bottom plates for the slide box simulations.

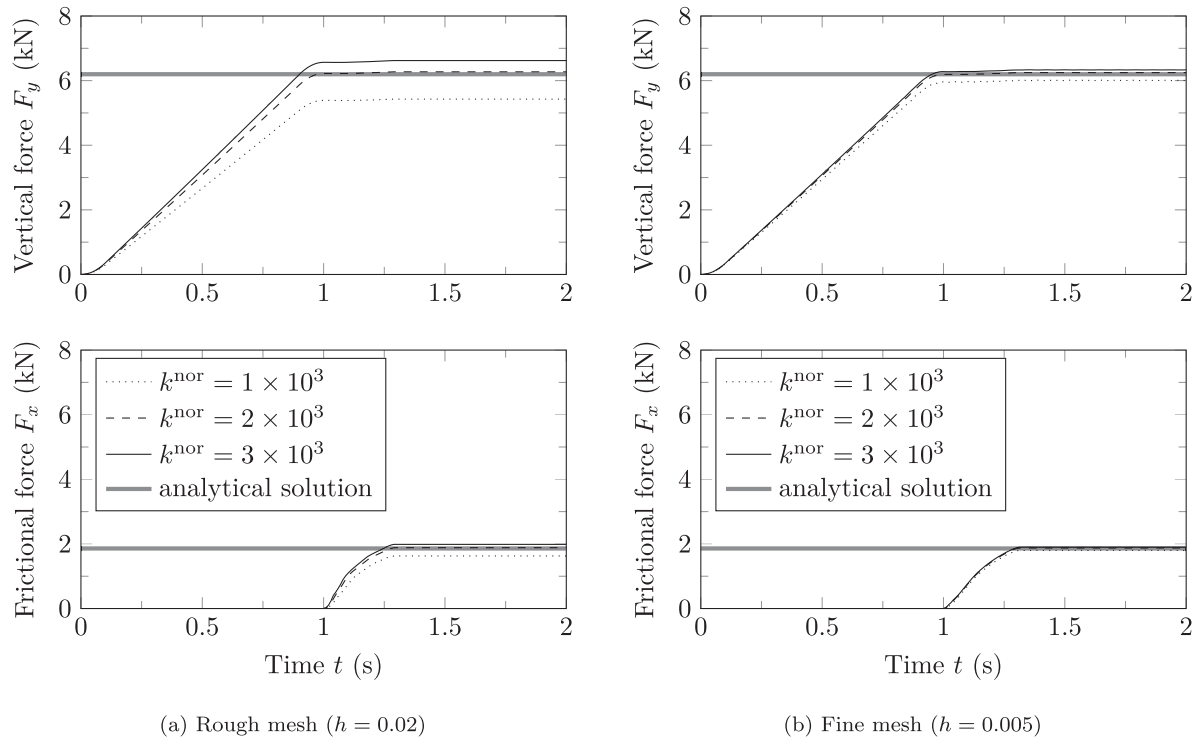


Fig. 8. Magnitude of the vertical and frictional forces acting on the bottom plate.

the presented formulation is reduced to the same form. Our contribution includes the generalization of the algorithm (Hu et al., 2018) for handling the boundary condition and frictional contact with rigid bodies. We summarize the comparison of the MPM (Sulsky et al., 1994) and WLS-MPM equations in Table 1.

## 6. Numerical simulations

In this section, three series of numerical simulations are presented to validate the proposed contact algorithm. The first set of simulations involves a sliding box for determining the effect of the penalty stiffness  $k^{nor}$  and the grid resolution. In the second set, a disk rolling on an inclined plane is observed. This simple example has been used extensively (Bardenhagen et al., 2000; Bardenhagen et al., 2001; Huang et al., 2011; Hamad et al., 2017) to validate frictional contact algorithms. In the third, the proposed algorithm is compared with finite element simulations using the strip footing problem.

### 6.1. Slide box

Fig. 6 shows the geometry of the slide box simulation, where the sample is a  $0.1 \text{ m} \times 0.1 \text{ m}$  square. The bottom plate is rough, with a friction coefficient  $\mu$ , whereas the other plates are smooth. In the simulation, the top plate initially moves down with a velocity  $v_y$  until the prescribed displacement is obtained; the bottom plate then slides with a velocity  $v_x$ . In order to reduce the stress oscillation of the material, the velocity of the top plate is controlled linearly from 0 to 0.5 mm/s in 0.1 s, maintained constant for 0.8 s, and decreased in 0.1 s. Similarly, the bottom plate is controlled linearly from 0 to 0.5 mm/s for 0.1 s and maintained constant, as shown in Fig. 7. As all the plates (except for the bottom one) have smooth surfaces, the frictional force  $F_x$  can be obtained using the vertical force  $F_y$ , as  $F_x = \mu F_y$ . The vertical force can be calculated assuming that the material body behaves as an element.

For the material points, we use a linear elastic model with the Young's modulus  $E = 10^3 \text{ kPa}$ , Poisson's ratio  $\nu = 0.3$ , and density  $10^3 \text{ kg/m}^3$ . The friction coefficient of the bottom plate is set to  $\mu = 0.3$ .

As the penalty stiffness depends on the material stiffness and grid refinement, we compare the results with  $k^{nor} = 1 \times 10^3, 2 \times 10^3, 3 \times 10^3 \text{ kN/m}$ , and two types of rough ( $h = 0.02 \text{ m}$ ) and fine ( $h = 0.005 \text{ m}$ ) grids. In the initial state, the number of particles per cell  $N_p$  is 4.

Fig. 8 depicts the magnitude of the vertical and frictional forces acting on the bottom plate. These forces are calculated as the summation of the nodal contact force  $f_i^c$ . From Fig. 8a, it can be inferred that the forces are weaker when  $k^{nor} = 1 \times 10^3$  and considerable when  $k^{nor} = 3 \times 10^3 \text{ kN/m}$ . The best accuracy can be obtained using  $k^{nor} = 2 \times 10^3 \text{ kN/m}$ . Accuracy improvement can also be achieved using a fine mesh as shown in Fig. 8b. In this case, for various penalty stiffness values, a good agreement with the analytical solution is observed. Thus, in order to obtain results with the desired accuracy, it is necessary to use a sufficiently fine mesh or select an appropriate value for the penalty

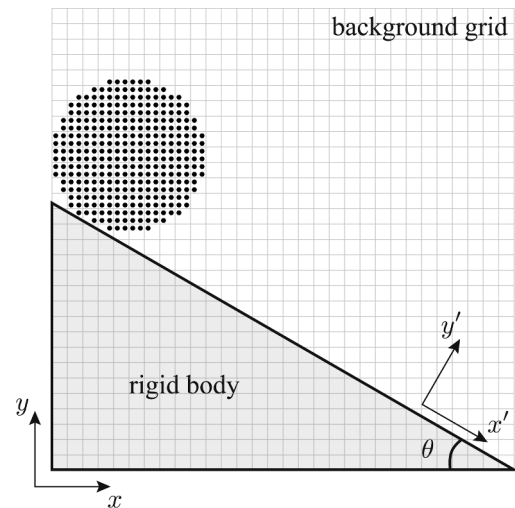
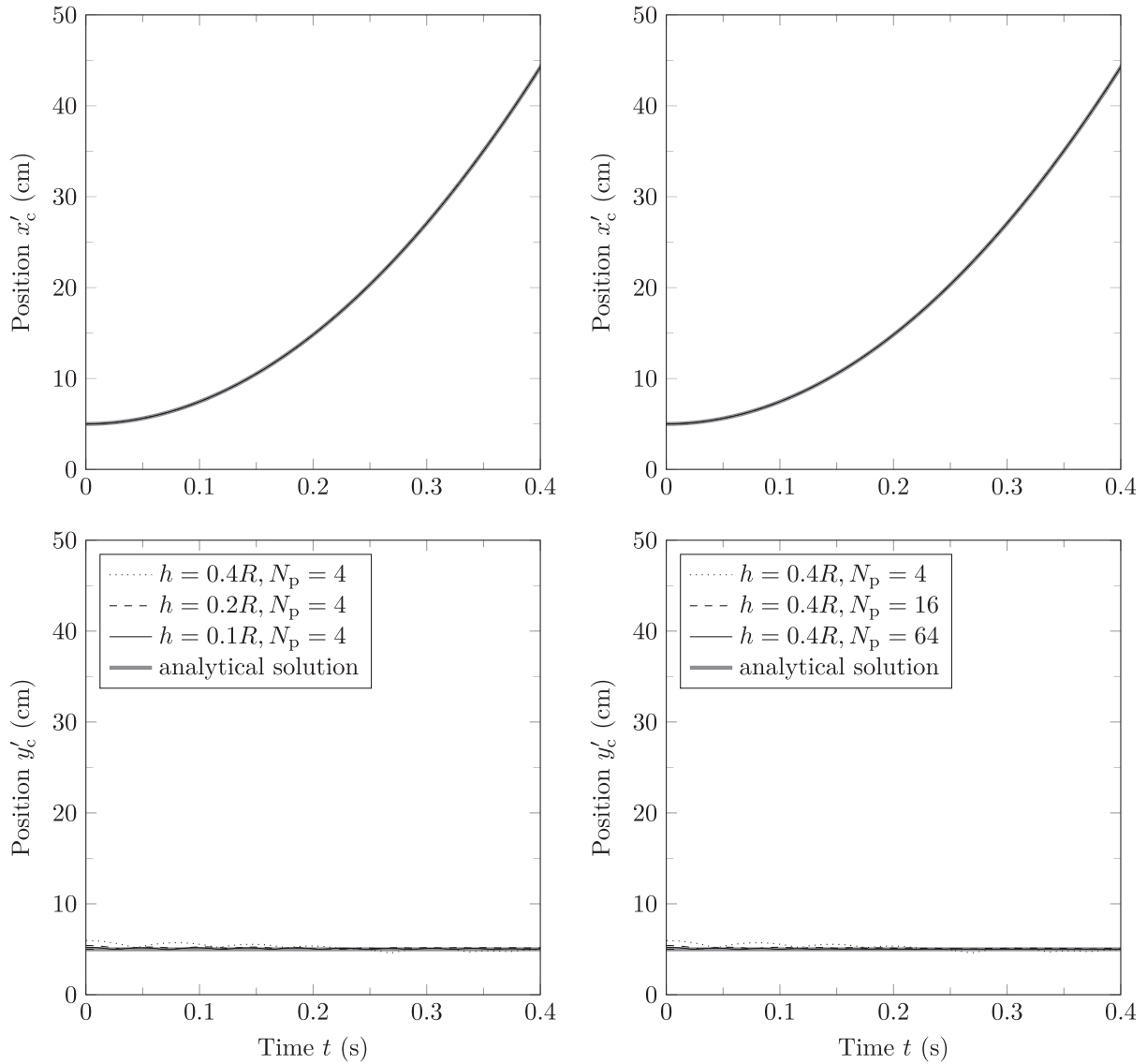


Fig. 9. Geometry for simulation of a disk on an inclined plane. The material point arrangement is the same as that for a mesh with  $h = 0.2R$ .





(a) Effect of grid resolution.

(b) Effect of the number of particles per cell.

**Fig. 10.** Center-of-mass position in the disk rolling simulation with a slip condition.

stiffness  $k^{\text{nor}}$  through sensitivity analysis. A more appropriate form of the normal contact force (28) or a method for reasonably determining the penalty stiffness  $k^{\text{nor}}$  is worth investigating.

## 6.2. Disk rolling on an inclined plane

Fig. 9 shows the simulation geometry. The plane is inclined at angle  $\theta$  with respect to the horizontal direction; the inclined plane is expressed as the side of a triangular object. If the disk can be considered rigid, the analytical solutions for the stick and slip contact cases can be determined using a combination of the angle of inclination  $\theta$  and friction coefficient  $\mu$ :

$$x'_c(t) = \begin{cases} x'_0 + \frac{1}{2}gt^2(\sin\theta - \mu\cos\theta), & \tan\theta > 3\mu \quad (\text{slip}) \\ x'_0 + \frac{1}{3}gt^2\sin\theta, & \tan\theta \leq 3\mu \quad (\text{stick}) \end{cases}, \quad (51)$$

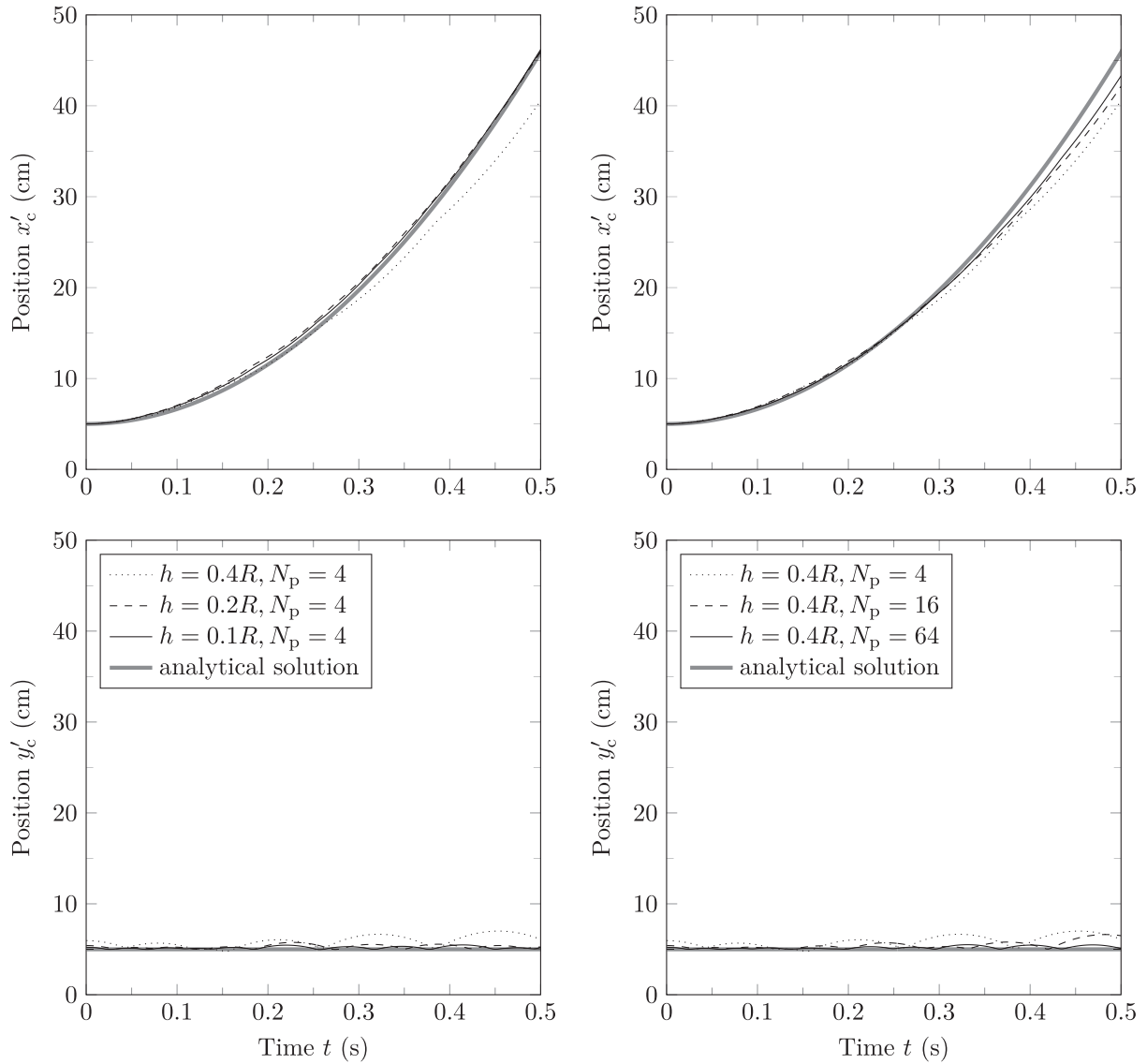
where  $x'_c$  is the center-of-mass position along the  $x'$  axis.

In the simulations, a disk of radius  $R = 0.05$  m is expressed as linear

elastic material points with the Young's modulus  $E = 10^3$  kPa, Poisson's ratio  $\nu = 0.3$ , and density  $\rho = 10^3$  kg/m<sup>3</sup>. The simulations are performed with three types of the grid spacing  $h = 0.4R, 0.2R, 0.1R$ . In addition, the number of particles per cell  $N_p$  is varied to determine the effect of the disk resolution. The angle of inclination  $\theta$  is set to  $\theta = 30^\circ$ . The friction coefficients are  $\mu = 0$  (slip) and  $\mu = 0.3$  (stick). The penalty stiffness is set to  $k^{\text{nor}} = 2 \times 10^3$  kN/m.

Fig. 10 displays the center-of-mass position  $x'_c$  for the slip case. In Fig. 10a, an excellent agreement with the analytical solution is observed even for a coarse mesh ( $h = 0.4R$ ), although the accuracy can be improved further on refining the mesh. Moreover, an improvement is realized by increasing the number of material points per cell (Fig. 10b). Fig. 11 shows the center-of-mass position  $x'_c$  for the stick case. Unlike the slip case, for the stick case, a low accuracy is observed for the coarse mesh (Fig. 11a); however, for the fine mesh, the results compare well with the analytical solution. In addition, using numerous particles improves the accuracy of the simulation, as shown in Fig. 11b.

In this example, we observed that the proposed contact algorithm works well in the slip contact condition. In contrast, when the frictional condition is applied, the result is more dependent on the spatial



(a) Effect of grid resolution.

(b) Effect of the number of particles per cell.

**Fig. 11.** Center-of-mass position in the disk rolling simulation with a stick condition.

resolution. For example, the results with low accuracy in Fig. 11a are due to the bouncing of the disk on the plane and because of the low spatial resolution of the disk (i.e., bumpy disk). This behavior does not occur in the slip case (Fig. 10a) because the disk slips (and does not roll) on the plane. As contact detection is implemented directly between the particle and rigid surface in the proposed contact algorithm, the arrangement/number of particles may have more effect on its results than on those of grid-based contact algorithms (Bardenhagen et al., 2000; Bardenhagen et al., 2001).

### 6.3. Strip footing

In this section, we validated the proposed algorithm by comparing the obtained solutions with those of finite element simulations using the commercial software PLAXIS. Firstly, we evaluate the MPM and FEM simulations using the strip footing problem while neglecting the weight of the soil and applying the von Mises model. We then use the Prandtl solution (Chen, 2013), which is a well-known analytical solution to this problem. Further, we compare the MPM solutions with those of the FEM, considering the weight of the soil with both rough and smooth footing.

As there are no theoretical values in this problem, the FEM results are, by themselves, regarded as the analytical solution. The geometry and boundary conditions of the strip footing problem are shown in Fig. 12. As it is symmetrical, only half the space is simulated.

#### 6.3.1. Bearing capacity of the strip footing neglecting the soil weight

The analytical solution for the bearing capacity given by Prandtl is

$$q_u = (2 + \pi)cB, \quad (52)$$

where  $c$  is the cohesion of the soil and  $B$  is the footing width. In the MPM and FEM simulations, we apply the von Mises model with linear elastic material. The yield function of the von Mises model is

$$\mathcal{F}(\boldsymbol{\sigma}) = \sqrt{3J_2(\boldsymbol{\sigma})} - \sigma_Y = 0, \quad (53)$$

where  $J_2$  is the second deviatoric stress invariant and  $\sigma_Y > 0$  is the material constant for the yield stress. In the plane strain condition, the yield stress  $\sigma_Y$  is related to the cohesion  $c$  in the Mohr–Coulomb failure criterion as follows:

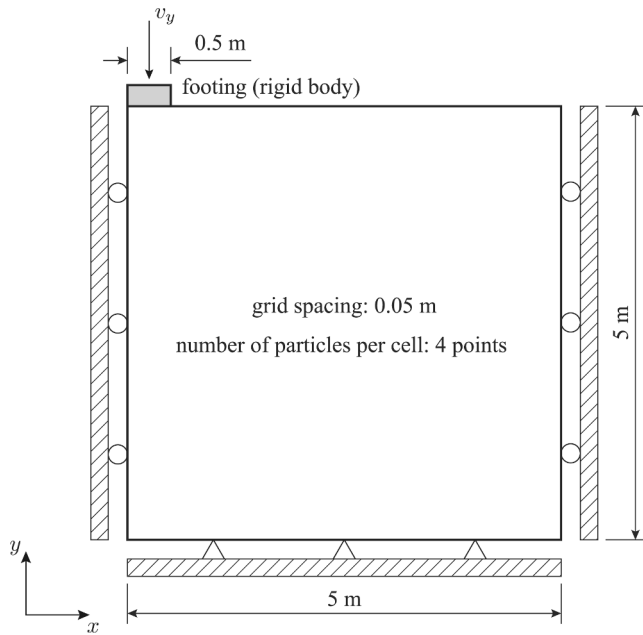


Fig. 12. Geometry and boundary conditions of the strip footing problem.

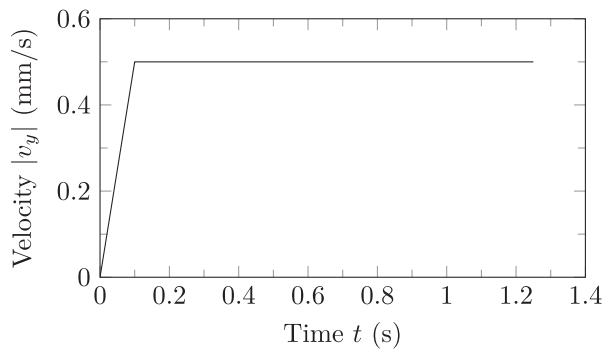


Fig. 13. Controlled velocity of the footing in the weightless-soil case.

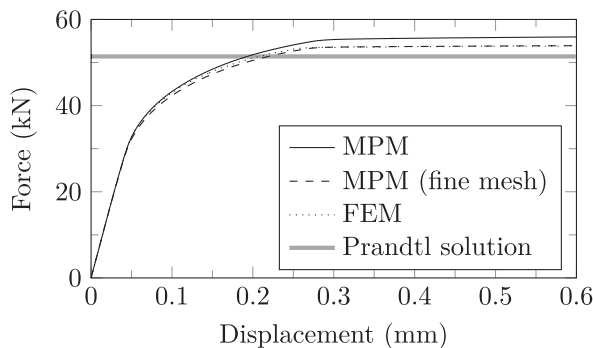


Fig. 14. Bearing capacity of the strip footing, neglecting the soil weight, and employing the von Mises model. In the fine mesh case for MPM, the grid spacing is set to 0.025 m.

$$\sigma_Y = \sqrt{3}c. \quad (54)$$

For the evolution of plastic strain, an associative flow rule is employed.

In order to reduce the stress oscillation of the material, the velocity of the footing is controlled linearly from 0 to 0.5 mm/s in 0.1 s and is maintained constant until the total displacement reaches 0.6 mm, as

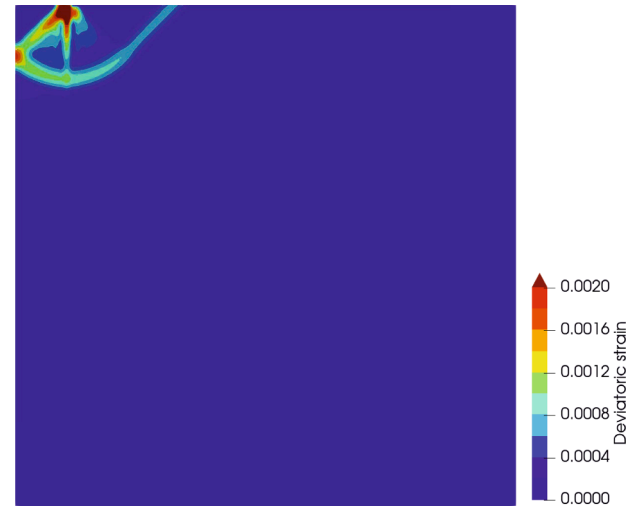


Fig. 15. Distribution of the deviatoric strain for the strip footing problem, neglecting the soil weight and applying the von Mises model in the MPM.

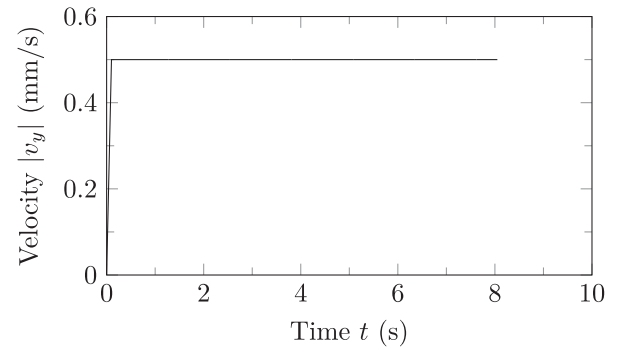


Fig. 16. Controlled velocity of the footing for the Drucker–Prager case.

shown in Fig. 13. Since this velocity is determined such that the particle acceleration is negligibly small, the effect of loading rate on the bearing capacity is ignored in this study. The material parameters of the ground are as follows: Young's modulus  $E = 10^6$  kPa, Poisson's ratio  $\nu = 0.3$ , density  $\rho = 10^3$  kg/m<sup>3</sup>, and cohesion  $c = 10$  kPa. In the MPM as well as FEM, smooth contact between the footing and ground is employed. It must be noted that for weightless soil, the bearing capacity with the rough condition is the same as that with the smooth condition. The penalty stiffness is set to  $k^{\text{nor}} = 2 \times 10^6$  kN/m.

Fig. 14 shows the bearing capacity of the strip footing, neglecting the soil weight. The MPM and FEM solutions show relatively stiffer behavior than the Prandtl solution. In order to improve the accuracy of the results, using a fine mesh is more advisable, as shown in Fig. 14 (see also Fatemizaddeh et al. (2015)). The distribution of the deviatoric strain (Fig. 15) shows the expected slip lines based on a Prandtl-type failure mechanism (Chen, 2013).

### 6.3.2. Bearing capacity of the strip footing considering the soil weight

As both the MPM and FE simulations show good agreement with the Prandtl solution (Fig. 14), we then validate the proposed frictional contact algorithm for the MPM by comparing it with the FE simulations. The geometry and boundary conditions are the same as in Fig. 12, with a change only in the application of the Drucker–Prager model for the ground, considering soil weight. The yield function of the Drucker–Prager model is

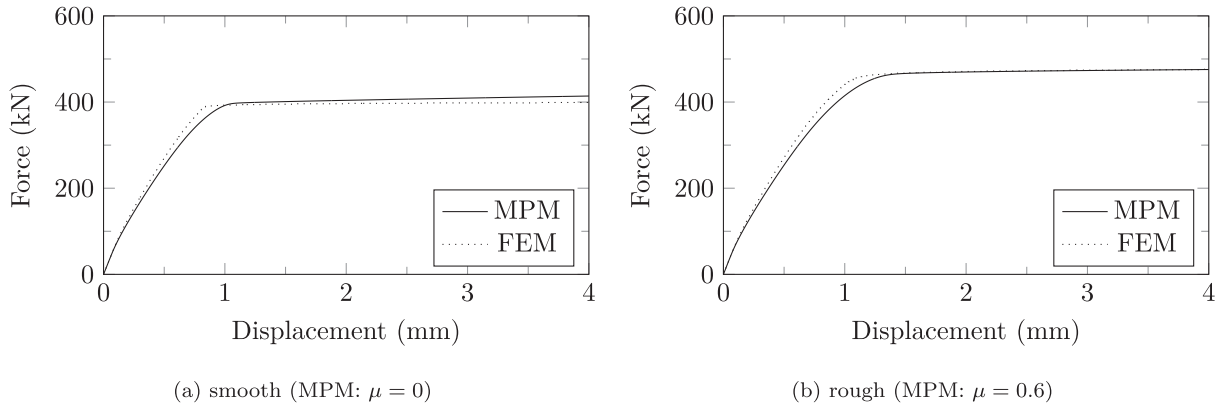


Fig. 17. Bearing capacity of the strip footing through the WLS-MPM and FEM.

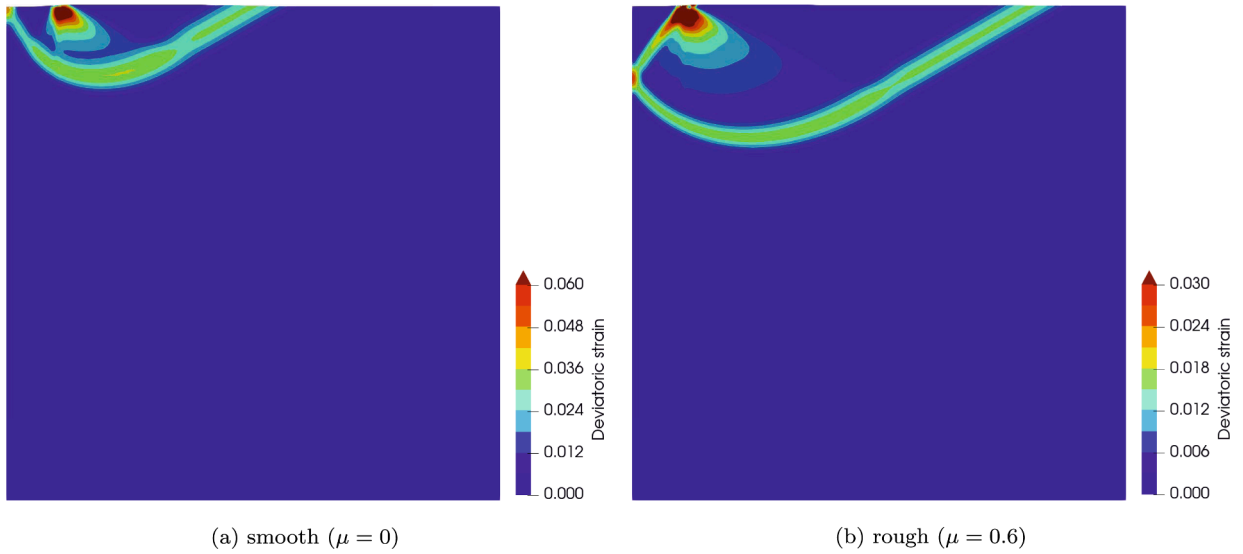


Fig. 18. Distribution of the deviatoric strain: (a) Hill-type failure mechanism in the smooth footing and (b) Prandtl-type failure mechanism in the rough footing.

$$\mathcal{F}(\sigma) = \sqrt{J_2(\sigma)} + \alpha I_1(\sigma) - \kappa = 0, \quad (55)$$

where  $I_1$  is the first stress invariant.  $\alpha$  and  $\kappa$  are material parameters related to the cohesion  $c$  and internal friction angle  $\phi$ , respectively, in the Mohr–Coulomb model. In the plane-strain condition, the material parameters are obtained as

$$\alpha = \frac{\tan \phi}{\sqrt{9 + 12 \tan^2 \phi}}, \quad \kappa = \frac{3c}{\sqrt{9 + 12 \tan^2 \phi}}. \quad (56)$$

For the evolution of plastic strain, the associative flow rule is employed.

Similarly in this case, to reduce the stress oscillation of the material, the velocity of the footing is controlled linearly from 0 to 0.5 mm/s in 0.1 s and is maintained constant until the total displacement reaches 4 mm, as shown Fig. 16. The material parameters of the ground are taken as follows: Young's modulus  $E = 10^6$  kPa, Poisson's ratio  $\nu = 0.3$ , density  $\rho = 10^3$  kg/m<sup>3</sup>, cohesion  $c = 10$  kPa, and internal friction angle  $\phi = 30^\circ$ . The vertical stress  $\sigma_y$  and horizontal stress  $\sigma_x$  are initialized as follows:

$$\sigma_y = \rho g H, \quad \sigma_x = \sigma_y \frac{\nu}{1 - \nu}, \quad (57)$$

where  $H$  is the depth from the ground surface and  $g$  is the acceleration due to gravity. In the FEM, the contact between the footing and ground is considered as the boundary condition, i.e., the constraints along the

horizontal direction are free for the smooth condition and fixed for the rough condition. On the other hand, in the MPM, we use the friction coefficient  $\mu = 0$  for the smooth condition and  $\mu = 0.6$  for the rough condition. The penalty stiffness is set to  $k^{\text{nor}} = 2 \times 10^6$  kN/m.

Fig. 17 depicts the bearing capacity of the strip footing considering the soil weight. For both smooth and rough conditions, the MPM results are in excellent agreement with those of the FEM. In the deviatoric strain distribution shown in Fig. 18, reasonable failure mechanisms such as the Hill-type failure mechanism in the smooth condition and the Prandtl-type failure mechanism in the rough condition are observed as reported by Griffiths et al. (2002).

## 7. Conclusions

A particle-to-surface frictional contact algorithm for the MPM was proposed in this study. In order to achieve precise contact detection, the proposed approach adopts the penalty method directly between the particle and surface, instead of the multivelocity field technique (Barndenhagen et al., 2000). Inconsistent transfers, wherein physical quantities may be mapped from the particles to grid nodes located within the rigid bodies, was resolved using the weighted least squares scheme (WLS-MPM). In this scheme, such invalid nodes are deactivated for constructing the shape functions without forfeiting the partition-of-unity property. As the WLS-MPM retains the delta function property on the boundary, the essential boundary conditions can be considered

similar to those of the original MPM.

The proposed algorithm was subsequently validated using three numerical simulation series. In all the simulations, the algorithm agreed well with the analytical and FEM solutions. However, the slide-box simulation indicated that in order to obtain results with the desired accuracy, it is necessary to use a sufficiently fine mesh or select an appropriate value of penalty stiffness using sensitivity analysis, similar to other algorithms based on the penalty method. A more appropriate method to compute the normal contact force or reasonably determine the penalty stiffness is worth investigating. The disk-rolling simulation demonstrated that the arrangement/number of particles may affect the results of the proposed algorithm more than those of the grid-based contact algorithms (Bardenhagen et al., 2000, 2001) as we implemented the contact detection directly between the particle and rigid surface. The strip footing simulations demonstrated that the proposed algorithm can successfully simulate the difference in bearing capacity of rough/smooth footing as well as the failure mechanisms in the ground.

Although the rigid body is given and known in this study (i.e., one-way coupling), two-way coupling can also be achieved by applying contact force to the rigid body. As the proposed method is based on the particle-to-surface contact algorithm, it is highly compatible with MPM–DEM or MPM–FEM coupled simulations, which we intend to explore in future research.

#### CRedit authorship contribution statement

**Keita Nakamura:** Conceptualization, Methodology, Software, Writing - original draft, Funding acquisition. **Satoshi Matsumura:** Writing - review & editing, Funding acquisition. **Takaaki Mizutani:** Writing - review & editing, Project administration.

#### Declaration of Competing Interest

The authors declare that they have no known competing financial interests or personal relationships that could have appeared to influence the work reported in this paper.

#### Acknowledgement

This work was supported by a research grant from the Japan Iron and Steel Federation and JSPS Grant-in-Aid for Early-Career Scientists [Project No. 19K15093] provided to the corresponding author.

#### References

- Bardenhagen, S., Brackbill, J., Sulsky, D., 2000. The material-point method for granular materials. *Comput. Methods Appl. Mech. Eng.* 187, 529–541.
- Bardenhagen, S., Guilkey, J.E., Roessig, K., Brackbill, J., Witzel, W., Foster, J., 2001. Improved contact algorithm for the material point method and application to stress propagation in granular material.
- Bardenhagen, S.G., Kober, E.M., 2004. The generalized interpolation material point method. *Comput. Model. Eng. Sci.* 5, 477–496.
- Belytschko, T., Lu, Y.Y., Gu, L., 1994. Element-free galerkin methods. *Int. J. Numer. Methods Eng.* 37, 229–256.
- Chen, W.F., 2013. Limit analysis and soil plasticity. Elsevier.
- Chen, Z., Qiu, X., Zhang, X., Lian, Y., 2015. Improved coupling of finite element method with material point method based on a particle-to-surface contact algorithm. *Comput. Methods Appl. Mech. Eng.* 293, 1–19.
- Chen, Z.P., Zhang, X., Qiu, X.M., Liu, Y., 2017. A frictional contact algorithm for implicit material point method. *Comput. Methods Appl. Mech. Eng.* 321, 124–144.
- Cheon, Y.J., Kim, H.G., 2018. An efficient contact algorithm for the interaction of material particles with finite elements. *Comput. Methods Appl. Mech. Eng.* 335, 631–659.
- Courant, R., Friedrichs, K., Lewy, H., 1967. On the partial difference equations of mathematical physics. *IBM J. Res. Develop.* 11, 215–234.
- Fatemizaddeh, S., Hamad, F., Moormann, C., 2015. Effects of the mpm discretisations on soil-structure problems. In: *PARTICLES IV: proceedings of the IV International Conference on Particle-Based Methods: fundamentals and applications, CIMNE*, pp. 635–645.
- Griffiths, D., Fenton, G.A., Manoharan, N., 2002. Bearing capacity of rough rigid strip footing on cohesive soil: probabilistic study. *J. Geotech. Geoenviron. Eng.* 128, 743–755.
- Hamad, F., Giridharan, S., Moormann, C., 2017. A penalty function method for modelling frictional contact in mpm. *Procedia Eng.* 175, 116–123.
- Harlow, F.H., 1964. The particle-in-cell computing method for fluid dynamics. *Methods Comput. Phys.* 3, 319–343.
- Hu, Y., Fang, Y., Ge, Z., Qu, Z., Zhu, Y., Pradhana, A., Jiang, C., 2018. A moving least squares material point method with displacement discontinuity and two-way rigid body coupling. *ACM Trans. Graph. (TOG)* 37, 1–14.
- Huang, P., Zhang, X., Ma, S., Huang, X., 2011. Contact algorithms for the material point method in impact and penetration simulation. *Int. J. Numer. Methods Eng.* 85, 498–517.
- Jiang, C., Schroeder, C., Selle, A., Teran, J., Stomakhin, A., 2015. The affine particle-in-cell method. *ACM Trans. Graph. (TOG)* 34, 1–10.
- Jiang, W., Zheng, H., 2011. Discontinuous deformation analysis based on variational inequality theory. *Int. J. Comput. Methods* 8, 193–208.
- Klár, G., Gast, T., Pradhana, A., Fu, C., Schroeder, C., Jiang, C., Teran, J., 2016. Drucker-prager elastoplasticity for sand animation. *ACM Trans. Graph. (TOG)* 35, 1–12.
- Lemiale, V., Nairn, J., Hurman, A., 2010. Material point method simulation of equal channel angular pressing involving large plastic strain and contact through sharp corners.
- Lian, Y., Zhang, X., Liu, Y., 2011. Coupling of finite element method with material point method by local multi-mesh contact method. *Comput. Methods Appl. Mech. Eng.* 200, 3482–3494.
- Liu, C., Sun, Q., Zhou, G.G., 2018. Coupling of material point method and discrete element method for granular flows impacting simulations. *Int. J. Numer. Meth. Eng.* 115, 172–188.
- Liu, W.K., Jun, S., Zhang, Y.F., 1995. Reproducing kernel particle methods. *Int. J. Numer. Methods Fluids* 20, 1081–1106.
- Ma, J., Wang, D., Randolph, M., 2014. A new contact algorithm in the material point method for geotechnical simulations. *Int. J. Numer. Anal. Meth. Geomech.* 38, 1197–1210.
- Ma, Z., Zhang, X., Huang, P., 2010. An object-oriented mpm framework for simulation of large deformation and contact of numerous grains. *Comput. Model. Eng. Sci. (CMES)* 55, 61.
- Monaghan, J.J., Lattanzio, J.C., 1985. A refined particle method for astrophysical problems. *Astron. Astrophys.* 149, 135–143.
- Mukherjee, Y., Mukherjee, S., 1997. On boundary conditions in the element-free galerkin method. *Comput. Mech.* 19, 264–270.
- Nairn, J., 2013. Modeling imperfect interfaces in the material point method using multimaterial methods. *Comput. Model. Eng. Sci.* 1, 1–15.
- Sadeghirad, A., Brannon, R.M., Burghardt, J., 2011. A convected particle domain interpolation technique to extend applicability of the material point method for problems involving massive deformations. *Int. J. Numer. Methods Eng.* 86, 1435–1456.
- Shepard, D., 1968. A two-dimensional interpolation function for irregularly-spaced data. In: *Proceedings of the 1968 23rd ACM national conference*, pp. 517–524.
- Simo, J.C., Laursen, T., 1992. An augmented lagrangian treatment of contact problems involving friction. *Comput. Struct.* 42, 97–116.
- Steffen, M., Kirby, R.M., Berzins, M., 2008. Analysis and reduction of quadrature errors in the material point method (mpm). *Int. J. Numer. Methods Eng.* 76, 922–948.
- Sulsky, D., Chen, Z., Schreyer, H.L., 1994. A particle method for history-dependent materials. *Comput. Methods Appl. Mech. Eng.* 118, 179–196.
- Sulsky, D., Zhou, S.J., Schreyer, H.L., 1995. Application of a particle-in-cell method to solid mechanics. *Comput. Phys. Commun.* 87, 236–252.
- Tran, Q.A., Wobbes, E., Solowski, W., Möller, M., Vuik, C., 2019. Moving least squares reconstruction for b-spline material point method.
- Wang, J., Chan, D., 2014. Frictional contact algorithms in sph for the simulation of soil–structure interaction. *Int. J. Numer. Anal. Meth. Geomech.* 38, 747–770.
- Zheng, H., Zhang, P., Du, X., 2016. Dual form of discontinuous deformation analysis. *Comput. Methods Appl. Mech. Eng.* 305, 196–216.